CCFE-PR(15)89

Y. Camenen, F.J. Casson, P. Manas, and A.G. Peeters

Turbulence stabilisation from the synergy between toroidal flow, parallel flow shear and perpendicular flow shear in tokamak plasmas

Enquiries about copyright and reproduction should in the first instance be addressed to the Culham Publications Officer, Culham Centre for Fusion Energy (CCFE), K1/0/83, Culham Science Centre, Abingdon, Oxfordshire, OX14 3DB, UK. The United Kingdom Atomic Energy Authority is the copyright holder.

Turbulence stabilisation from the synergy between toroidal flow, parallel flow shear and perpendicular flow shear in tokamak plasmas

Y. Camenen,[1] F.J. Casson,[2] P. Manas,[1] and A.G. Peeters[3]

[1]CNRS, Aix-Marseille Université, PIIM UMR 7345, Marseille, France
[2]CCFE, Culham Science Centre, Abingdon, Oxon, OX14 3DB, United Kingdom
[3]University of Bayreuth, Physics Department, Universitätsstrasse 30, Bayreuth, Germany

Further reproduction distribution of this paper is subject to the journal publication rules.

Turbulence stabilisation from the synergy between toroidal flow, parallel flow shear and perpendicular flow shear in tokamak plasmas

Y. Camenen,[1,*] F.J. Casson,[2] P. Manas,[1] and A.G. Peeters[3]
[1] *CNRS, Aix-Marseille Université, PIIM UMR 7345, Marseille, France*
[2] *CCFE, Culham Science Centre, Abingdon, Oxon, OX14 3DB, United Kingdom*
[3] *University of Bayreuth, Physics Department, Universitätsstrasse 30, Bayreuth, Germany*

The interplay between toroidal rotation u, parallel flow shear u' and perpendicular flow shear γ_E in the stabilisation of tokamak turbulence is investigated in non-linear flux-tube gyrokinetic simulations with the GKW code. The non-linear simulations are performed for a reference L-mode DIII-D plasma (the so-called shortfall case) at $r/a = 0.8$, varying the flow parameters around their nominal values. Depending on the respective signs of u, u' and γ_E, turbulence is found to be enhanced, reduced or unchanged. When the coupling is favorable, the overall effect on the non-linear heat fluxes can be very large, even at moderate flow values. The ion heat flux is for instance decreased by a factor of three when the direction of the parallel flow shear is reversed with respect to its nominal value. Even more surprising, keeping u' and γ_E at their nominal values, the ion heat flux decreases by more than 50% when the toroidal flow is reversed. The relevance of this mechanism in the experiments, which depends on the ability to decouple u, u' and γ_E is discussed.

PACS numbers:

I. INTRODUCTION

Sheared flows have long been known to play an important role in the regulation of turbulence. Basically, two mechanisms are at play: on one side, the plasma advection by sheared flows tends to decorrelate the turbulent structures and decrease the turbulence saturation level, whereas on the other side sheared flows have a direct impact on linear modes that makes them more or less unstable depending on the cases [1]. For core tokamak plasma turbulence, the strong scale separation in the directions parallel and perpendicular to the magnetic field, typically $k_\parallel/k_\perp \sim qR/\rho_i \gg 1$ (with q the safety factor, R the major radius of the torus and ρ_i the ion Larmor radius), makes the shear in the perpendicular flow much more effective to decorrelate turbulent structures than the shear in the parallel flow. As a result, a radial shear in the perpendicular flow is usually stabilising, see e.g. [2], whereas the main effect of a radial shear in the parallel flow is to drive the parallel velocity gradient (PVG) instability [3, 4]. In the limit of pure toroidal rotation, a reasonable assumption in the plasma core in the absence of transport barriers, the perpendicular and parallel flows are geometrically linked by the ratio between the poloidal and toroidal magnetic field B_p/B_t (scaling as ε/q for circular flux surfaces at low inverse aspect ratio ε). When the toroidal flow shear increases, its perpendicular and parallel components increase in proportion and their impact on the turbulence is weighted according to the value of B_p/B_t: at large B_p/B_t, the perpendicular to parallel flow shear ratio is larger than at low B_p/B_t and stabilisation is favored, the opposite being true at small B_p/B_t [5–7]. Recently, the impact of the toroidal flow itself on turbulence regulation has also been investigated. At low Mach number, the toroidal flow barely affects the turbulence saturation. However, for toroidal Mach numbers nearing or exceeding unity, ion temperature gradient and trapped electron mode turbulence is found to increase significantly with toroidal rotation, due to an increase of the linear trapped electron mode drive and to a reduced zonal flow residual induced by the centrifugal force [8].

The present work aims at investigating the interplay between toroidal rotation, parallel flow shear and perpendicular flow shear in turbulence stabilisation. The study is motivated by the unexpectedly strong impact of the toroidal flow on the non-linear heat fluxes observed at low Mach number with the gyrokinetic Eulerian code GKW [9] in the frame of a multi-code benchmark effort based on the DIII-D L-mode shortfall case [10].

In the following, the treatment of plasma flows in GKW is first presented, together with a brief reminder of the scaling of neoclassical flows in tokamaks. A simple fluid dispersion relation is then derived to highlight the coupling between toroidal rotation and parallel flow shear in the linear stability of the toroidal Ion Temperature Gradient mode (ITG). Guided by the fluid model results, the impact of the cross-term on the linear mode growth rate and its parametric dependencies are investigated in linear simulations. The impact of the flow parameters on the non-linear heat flux is then characterised and quantified in simulations based on the shortfall case. Finally, the relevance of this mechanism in the experiments is discussed and the results are summarized.

---

[*] Electronic address: `yann.camenen@univ-amu.fr`

II. TOKAMAK FLOWS AND THEIR DESCRIPTION IN GKW

A. Coordinate system and magnetic topology

To proceed with the description of the flows implementation in GKW, we first define a right-handed toroidal flux-coordinate system (r, θ, φ). The minor radius $r = \frac{1}{2}(R_{\rm min} + R_{\rm max})$ is a flux surface label, with $R_{\rm min}$ and $R_{\rm max}$ the minimum and maximum major radii of the flux surface, respectively. The poloidal angle θ is zero at the low field side midplane and increases towards the top of the torus. The toroidal angle φ is clockwise when viewed from above.
As is customary, the axisymmetric equilibrium magnetic field is expressed as:

$$\mathbf{B} = s_b F \nabla\varphi + s_j \nabla\varphi \times \nabla\psi \tag{1}$$

where $F = RB_t > 0$ and ψ is the poloidal magnetic flux. Note that the direction of the toroidal magnetic field and plasma current, s_b and s_j respectively (positive when clockwise from above), have been singled out in the expression of the magnetic field. As a consequence, all scalar quantities related to the magnetic field (the safety factor q for instance) are considered positive and the signs explicitely appear via s_b and s_j. Consistently with Eq. (1), the poloidal magnetic flux ψ is minimum on the magnetic axis and $\nabla\psi$ points in the same direction as ∇r.

B. Neoclassical flows

By ordering the radial flow small compared to the flow within a flux surface and projecting the poloidal flow into the parallel and toroidal directions, the flow of species s can be expressed as [11]:

$$\mathbf{V}_s = \hat{u}_{\theta,s}\mathbf{B} + R^2(\omega_{p,s} + \omega_\Phi)\nabla\varphi \tag{2}$$

where

$$\begin{aligned} \hat{u}_{\theta,s} &= \frac{\mathbf{V}_s \cdot \nabla\theta}{\mathbf{B}\cdot\nabla\theta} & (3)\\ \omega_{p,s} &= -\frac{s_j}{Z_s e n_s}\frac{\partial p_s}{\partial\psi} & (4)\\ \omega_\Phi &= -s_j\frac{\partial\Phi}{\partial\psi} & (5) \end{aligned}$$

with Z_s, n_s and p_s the species charge number, density and pressure, respectively, and Φ the electrostatic potential. In tokamaks, the poloidal component of the flow is strongly constrained by neoclassical physics and damped towards a species dependent offset $\hat{u}_{\theta,s}^{\rm neo}$ on timescales of the order of the ion-ion collision frequency. For main ions, the poloidal neoclassical flow is given by

$$\hat{u}_{\theta,i}^{\rm neo} = -s_b s_j \frac{1}{2}\rho_* v_{\rm thi}\frac{\partial r}{\partial\psi}\frac{FB_0}{< B^2 >} k_i R/L_{T_i} \tag{6}$$

where $v_{\rm thi} = \sqrt{2T_i/m_i}$ is the ion thermal velocity, with T_i the ion temperature and m_i the ion mass, $\rho_* = m_i v_{\rm thi}/(eB_0R_0)$ is the normalised ion Larmor radius, with B_0 the reference magnetic field and R_0 the reference major radius, $R/L_{T_i} = -R_0\partial\log T_i/\partial r$ is the normalised ion temperature gradient and $< . >$ denotes the flux surface average. The flow coefficient k_i is dimensionless, typically of order unity, and depends on the plasma shape and collisionality (see [12] for typical dependencies on plasma parameters and comparisons between standard analytical limits and drift-kinetic simulations). In the banana regime (low collisionality), k_i is positive which corresponds to a poloidal velocity in the ion diamagnetic drift direction. Recasting Eq (4) to make the ρ_* dependence appear,

$$\omega_{p,i} = s_j\frac{1}{2}\rho_* v_{\rm thi}\frac{\partial r}{\partial\psi}B_0 R/L_{p_i} \tag{7}$$

shows that in the limit of vanishing ρ_*, the neoclassical flow is purely toroidal [13] and given by:

$$\mathbf{V}_i^{(0)} = \omega_\Phi R^2\nabla\varphi \tag{8}$$

with ω_Φ constant on a flux surface. The flow physics implemented in GKW relies on a plasma flow described by Eq. (8).

C. Implementation in GKW

GKW is an Eulerian δf gyrokinetic code. The version used in the present study assumes a Maxwellian background distribution function and is based on the gyrokinetic equations in the local approximation [9]. It describes the turbulence in a flux-tube wrapped around the flux surface labelled by $r = r_0$. In this description, the flow physics enters in three distinct ways: via the flow itself (inertial effects), via the shear in the parallel flow and via the shear in the $\mathbf{E}\times\mathbf{B}$ flow. The implementation of these three components is briefly outlined below. A comprehensive description of the equations can be found in the GKW manual [14] and their derivation in the electrostatic limit is given in [15, 16].

1. *Inertial effects*

GKW equations are formulated in a frame that rotates toroidaly as a rigid body [15, 16]. The angular frequency of the frame Ω is chosen to cancel the lowest order $\mathbf{E}\times\mathbf{B}$ drift at $r = r_0$ and is defined positive for a plasma flow in the direction of the toroidal magnetic field:

$$\Omega = s_b\omega_\Phi \tag{9}$$

The frame frequency is specified in the code via the normalised toroidal velocity u defined as:

$$u = \frac{R_0}{v_{\rm thi}}\Omega \tag{10}$$

In the rotating frame, the inertial effects associated to the background flow appear via the Coriolis and centrifugal forces. These two forces result in several modifications of the gyrokinetic equations presented in Appendix A. By definition of the frame frequency, all the inertial effects associated to the lowest order neoclassical flow given in Eq (8) are taken into account. Inertial effects associated to departures from the lowest order neoclassical flow (i.e. finite poloidal rotation and/or species dependent toroidal rotation) are neglected in the present implementation. In most of the simulations presented in this paper, the Coriolis drift is the only inertial effect taken into account, i.e. centrifugal effects are neglected.

2. Flow shear

The parallel flow shear is assumed to arise entirely from the shear in a toroidal flow of constant angular frequency on a flux surface. It enters the Maxwellian background as detailed in Appendix B 1. It is specified for each species by the normalised toroidal rotation u'_s defined as:

$$u'_s = -\frac{R_0^2}{v_{\rm thi}}\frac{\partial \omega_s^f}{\partial r} \tag{11}$$

where the species angular frequency in the rotating frame ω_s^f is assumed to be constant on a flux surface. In the present study, all species are considered to have the same parallel flow shear and this common flow shear is noted u'.

The advection by a sheared $\mathbf{E}\times\mathbf{B}$ flow is taken into account by linearising the $\mathbf{E}\times\mathbf{B}$ flow around $r = r_0$ (see Appendix B 2) and specified via the normalised $\mathbf{E}\times\mathbf{B}$ shearing rate:

$$\gamma_E = \frac{R_0}{v_{\rm thi}}\frac{1}{B_0}\frac{\partial^2\Phi^f}{\partial r^2} \tag{12}$$

where Φ^f is the lowest order electrostatic potential in the rotating frame.

3. Departure from purely toroidal flows

Strictly speaking, the flow treatment in GKW is only valid in the limit of a purely toroidal rotation described by Eq. (8). The parallel and $\mathbf{E}\times\mathbf{B}$ flow shears are then coupled and given by:

$$u'_s = -s_b\frac{R_0^2}{v_{\rm thi}}\frac{\partial\omega_\Phi}{\partial r} \tag{13}$$

$$\gamma_E = -s_j\frac{R_0}{B_0 v_{\rm thi}}\frac{\partial\psi}{\partial r}\frac{\partial\omega_\Phi}{\partial r} \tag{14}$$

In reality, tokamak flows are not purely toroidal and differ for each species, i.e. $\hat{u}_{\theta,s}$ and $\omega_{p,s}$ are finite in Eq. (2). Considering that the poloidal flow is neoclassical and described by Eq. (6), the departure from a purely toroidal flow scales as

$$\hat{u}_{\theta,i}B \sim \frac{1}{2}\rho_* v_{\rm thi}\frac{B_t}{B_p}R/L_{T_i}, \tag{15}$$

where $\partial\psi/\partial r = RB_p|\nabla r| \sim RB_p$ and $k_i \sim 1$ have been assumed. Provided the collisionality is slowly varying with the minor radius, the corresponding contribution to the flow shear then scales as

$$R_0 B\frac{\partial\hat{u}_{\theta,i}}{\partial r} \sim \frac{1}{2}\rho_* v_{\rm thi}\frac{B_t}{B_p}\left[R/L_{T_i}\right]^2 \tag{16}$$

where

$$\frac{R_0^2}{T_i}\frac{\partial^2 T_i}{\partial r^2} = \left[R/L_{T_i}\right]^2 + R_0\frac{\partial}{\partial r}\left[R/L_{T_i}\right] \sim \left[R/L_{T_i}\right]^2 \tag{17}$$

has been assumed and where the derivatives related to the magnetic equilibrium have been considered of order unity, e.g. $R_0\partial\ln B/\partial r \sim 1$.

For $\rho_* = 1/600$, $B_t/B_p \sim q/\epsilon = 10$ and $R/L_{T_i} = 6$, Eqs. (15) and (16) yield $\hat{u}_{\theta,i}B \sim 0.05\,v_{\rm thi}$ and $B\partial\hat{u}_{\theta,i}/\partial r \sim 0.3\,v_{\rm thi}/R_0$. These values are to be compared to the values of the toroidal flow, $0.1-0.4\,v_{\rm thi}$, and flow shear, $1-3\,v_{\rm thi}/R_0$, typically measured in the tokamak core. These estimates imply that the flow parameters corresponding to pure toroidal rotation are modified by some $10-40\%$ when neoclassical poloidal rotation is considered. For the modelling of experimental plasmas with a significant departure from purely toroidal sheared flows, the values of u'_s and γ_E can be specified as described in Appendix B 3. The assumption in Eq. (17) is rather conservative and in practice the second derivative of the temperature can easily be several times larger, especially in the case of internal transport barriers or closer to the plasma edge where R/L_{T_i} increases rapidly with the minor radius. It is with these cases in mind that the values of u'_s and γ_E are scanned independently in the present study.

III. IMPACT OF u AND u' ON THE LINEAR STABILITY OF THE TOROIDAL ITG

A. Insights from a simplified fluid model

Before moving to the simulation results, the interplay between toroidal rotation u and parallel flow shear u' in the linear stability of the toroidal Ion Temperature Gradient mode (ITG) is explored with a simple fluid model. The purpose of the model is to help interpreting the gyrokinetic simulations by emphasizing the mechanisms at play in a simplified framework.

A detailed derivation of the model can be found in [15]. For completeness, its main characteristics are reminded below. The model is built from the first three moments of the linearised gyrokinetic equation in the local δf approximation and evaluated at the low-field-side midplane (strong ballooning assumption). It assumes an adiabatic electron response, neglects finite Larmor radius effect and uses a Maxwellian closure. The magnetic field is considered to be purely toroidal with $s_b = -1$. In the following, the inertial effects associated to the Coriolis force are retained but centrifugal effects are neglected (they are retained in [15]). Singly charged ions $Z = 1$ with an equal ion and electron background temperature $T_i = T_e$ are considered. The complex mode frequency $\omega = \omega_R + i\gamma$, the parallel wave vector $k_\|$ and the perturbed electrostatic potential $\delta\phi$ are normalised as follows:

$$\hat{\omega} = \frac{\omega}{\omega_D}, \qquad \hat{k}_\| = \frac{1}{2}\frac{k_\| R}{k_z \rho_i}, \qquad \tilde{\phi} = \frac{e\delta\phi}{T_e} \tag{18}$$

with k_z the poloidal wavevector and $\omega_D = -k_z T_i/(eBR)$ the drift frequency. With these normalisations, the perturbations are moving in the electron diamagnetic drift direction for $\omega_R > 0$. The evolution of the ion normalised perturbed density $\tilde{n} = \delta n_i / n_i$, parallel fluid velocity $\tilde{w} = \delta v_{\|i}/v_{\mathrm{thi}}$ and temperature $\tilde{T} = \delta T_i / T_i$ is given by:

$$\hat{\omega}\tilde{n} + 2[\tilde{n} + \tilde{T}] + 4[u + \hat{k}_\|]\tilde{w} = \left[\frac{R}{L_n} - 2\right]\tilde{\phi} \tag{19}$$

$$\hat{\omega}\tilde{w} + 4\tilde{w} + 2[u + \hat{k}_\|][\tilde{n} + \tilde{T}] = \left[u' - 2u - 2\hat{k}_\|\right]\tilde{\phi} \tag{20}$$

$$\hat{\omega}\tilde{T} + \frac{4}{3}\tilde{n} + \frac{14}{3}\tilde{T} + \frac{8}{3}[u + \hat{k}_\|]\tilde{w} = \left[\frac{R}{L_{T_i}} - \frac{4}{3}\right]\tilde{\phi} \tag{21}$$

where the equation for the temperature has been obtained by subtracting Eq. (19) to the equation for the pressure. In the three equations above, the terms related to the perturbations are gathered on the left hand side, whereas the ones related to the background are on the right hand side. On the left hand side, one finds, in that order, the temporal derivative of the perturbation, the advection of the perturbation by 1) the curvature and ∇B drift, 2) the Coriolis drift (terms proportional to u) and 3) the parallel motion (terms proportional to $k_\|$). On the right hand side, one has the advection of the background by the $E \times B$ drift (terms involving the gradients of the background) and finally the advection in velocity space of the background (acceleration) due to the curvature and ∇B drift in the perturbed electric field for Eqs. (19) and (21) or to the Coriolis drift and parallel motion in the perturbed electric field for Eq. (20).

The Coriolis drift and the parallel dynamics couple parallel velocity fluctuations $\tilde{w}$ to density $\tilde{n}$ and temperature $\tilde{T}$ fluctuations. When this coupling is neglected ($u = 0$ and $\hat{k}_\| = 0$), Eqs. (19) and (21) yield the "standard" picture of the toroidal ITG. This picture is reminded here assuming $R/L_n = 2$ for simplicity. Starting from an initial temperature perturbation $\tilde{T}$, the advection by the curvature and ∇B drift generates an ion density perturbation (by compression):

$$\tilde{n} = -\frac{2}{\hat{\omega} + 2}\tilde{T} \tag{22}$$

Quasineutrality ($\delta n_e = \delta n_i$) and the adiabatic electron response imply that an electrostatic potential perturbation builds up in response to the density perturbation:

$$\tilde{\phi} = \tilde{n} \tag{23}$$

which in turn generates a temperature perturbation by $E \times B$ advection in the background temperature gradient:

$$\tilde{T} = \frac{1}{\hat{\omega} + 14/3}\left[\frac{R}{L_{T_i}} - \frac{8}{3}\right]\tilde{\phi} \tag{24}$$

Depending on the phase shift between $\tilde{T}$ and $\tilde{\phi}$, which is governed by the curvature and ∇B drifts, the perturbation will grow or not. This is best seen by computing the dispersion relation from Eqs (22-24):

$$\hat{\omega}^2 + \frac{20}{3}\hat{\omega} + 2\frac{R}{L_{T_i}} + 4 = 0 \tag{25}$$

and solving for the mode growth rate:

$$\gamma = k_z \rho_i \frac{v_{\mathrm{thi}}}{R_0}\sqrt{2\frac{R}{L_{T_i}} - \frac{64}{9}} \tag{26}$$

which shows that the mode requires a critical temperature gradient $R/L_{T_i} > 32/9$ to be unstable.

When the Coriolis drit and parallel dynamics are considered (finite u and $\hat{k}_\|$ values), additional density and temperature perturbations are generated by the parallel velocity perturbations. Eqs (22) and (24) then become:

$$\tilde{n} = -\frac{2}{\hat{\omega} + 2}\left[\tilde{T} - 2\left[u + \hat{k}_\|\right]\tilde{w}\right] \tag{27}$$

$$\tilde{T} = \frac{1}{\hat{\omega} + 14/3}\left[\left[\frac{R}{L_{T_i}} - \frac{8}{3}\right]\tilde{\phi} - \frac{8}{3}\left[u + \hat{k}_\|\right]\tilde{w}\right] \tag{28}$$

The impact on the mode stability depends on the phase of these new contributions to $\tilde{n}$ and $\tilde{T}$ with respect to the initial ones: for instance, do the density perturbations generated by the Coriolis drift and parallel compression add or subtract to the one generated by the curvature and ∇B compression? This depends on what mechanism drives the parallel velocity perturbations and the question is answered by computing $\tilde{w}$ with Eq. (20). The corresponding dispersion relation has been derived in [17] in the limit of marginaly unstable modes ($\gamma > 0$ and $\gamma \ll |\omega_R|$) and small symmetry breaking ($|u + \hat{k}_\|| \ll 1$). It yields to the following mode growth rate:

$$\gamma = \sqrt{\gamma_0^2 + a_1[u + \hat{k}_\|]u' + a_2[u + \hat{k}_\|]^2} \tag{29}$$

where the assumption $R/L_n = 2$ has been relaxed, γ_0 is the growth rate in the absence of flows (i.e. $u = 0$

and $u' = 0$, which in this limit imply $\hat{k}_\parallel = 0$) and the coefficients a_1 and a_2 are given by:

$$a_1 = -4\frac{R/L_n - 2}{R/L_n - 2/3}, \qquad a_2 = 2\left[\frac{R}{L_n} + \frac{26}{3}\right] \tag{30}$$

To get a closed expression for the mode growth rate in the presence of flows, the value of $\hat{k}_\parallel$ needs to be specified in Eq. (29). The kinetic electron response has been shown to be an essential ingredient in the parallel mode structure response to background flows [17] which makes the quantitative prediction of $\hat{k}_\parallel$ well beyond the scope of the simple fluid model used in this section, and in fact beyond the scope of any fluid model assuming an adiabatic electron response. Short of being accurate, the self-consistent parallel mode structure under the adiabatic electrons approximation is still of interest to investigate the dependencies of $\hat{k}_\parallel$ on the flow parameters. A calculation in this spirit has been done in [18] and shows that $\hat{k}_\parallel \propto u' - 2u$. Interestingly, this linear dependence of $\hat{k}_\parallel$ on u' and u with an opposite sign is recovered in gyrokinetic simulations, as shown in Fig. 3 of [19] and in Fig. 2 of the next section. Of course, the respective impact of u and u' is not always linked by a factor of 2 and departures from the linear dependence can also be observed. Nevertheless, assuming that $\hat{k}_\parallel$ is proportional to u and u' with an opposite sign qualitatively captures the main impact of flows on the parallel mode structure. With this assumption, Eq. (29) can be written as

$$\gamma = \sqrt{\gamma_0^2 + b_{u'}u'^2 + b_{uu'}uu' + b_u u^2} \tag{31}$$

where $b_{u'}$, $b_{uu'}$ and b_u are parameter dependent coefficients left unspecified. Eq. (31) highlights the quadratic dependence of the mode growth rate on the flow parameters.

In summary, the simple model tells us that toroidal rotation (u), parallel flow shear (u') and the parallel gradient of the perturbed pressure and electrostatic potential ($k_\parallel$) generate parallel velocity perturbations which modify the phase shift between temperature and density perturbation (and hence potential) via the coupling provided by the parallel compression and Coriolis drift. As a consequence, the ITG mode is made more or less stable. The overall effect depends on the respective signs of toroidal rotation u and parallel flow shear u', as emphasised in Eq. (31). The existence of a cross-term proportional to uu' implies that the parallel flow shear can have a stabilising effect. In the present section, the impact of $\mathbf{E} \times \mathbf{B}$ shearing was not discussed, but previous analytical works [20, 21] show the existence of a similar cross-term between u' and γ_E in the stability of the linear ITG.

B. Gyrokinetic simulations

The effect of u and u' on linear stability is now explored in gyrokinetic simulations for two cases. First, for the Waltz standard case [5], to characterize the parametric dependencies and emphasize the robustness of the mechanisms at play. Second, for the shortfall case at $r/a = 0.8$ and with zero electron temperature gradient, $R/L_{T_e} = 0$, for which all the non-linear simulations presented in this paper have been performed. The main input parameters for these two cases are gathered in Table I. No $\mathbf{E} \times \mathbf{B}$ shear flow is applied in the linear simulations.

	Waltz standard case	DIII-D shortfall case
R/L_{T_i}	9	7.0312
R/L_{T_e}	9	0
R/L_n	3	2.9903
T_e/T_i	1	0.8519
ϵ	0.16	0.2861
q	2	2.7660
$\hat{s}$	1	2.0500
u	0	-0.1549
u'	0	-1.2584
γ_E	0	-0.2106
β	0	8.077×10^{-4}
ν_{eff}	0	1.9302

TABLE I: Main input parameters for the two reference cases. The input definitions and normalisations can be found in [14].

1. Waltz standard case

For the Waltz standard case, the flux surfaces are concentric circles and only electrostatic perturbations are retained. The impact of the toroidal flow u and parallel flow shear u' on the linear mode growth rate is investigated for $k_\theta\rho_i = 0.4$ and $k_r\rho_i = 0$, near the peak of the mode growth rate. The variations of the growth rate as a function of u and u' are shown in Fig. 1. At zero toroidal rotation, the parallel flow shear is found to be destabilising, consistently with the conventional ITG-PVG coupling picture. However, as soon as the toroidal rotation is finite, the parallel flow shear can be stabilising or destabilising, depending on the sign of uu'. Conversely, at finite parallel flow shear, toroidal rotation can be stabilising or destabilising. The linear mode growth rate is maximum for positive uu' and minimum for negative uu' values, with a saddle point at $u = 0$ and $u' = 0$. Encouraged by the similarity of this behaviour with the prediction of the fluid model, a fit of the form given by Eq. (31) is attempted. The coefficients $b_{u'}$, $b_{uu'}$ and b_u are calculated from the growth rate values of the five cases given in Table II. The combination of cases 1 and 2 yields $b_u = -0.77$, cases 1 and 3 $b_{u'} = 0.0048$ and cases 4 and 5 $b_{uu'} = 0.14$. The resulting fit proves to be of rather good quality: the relative difference between the fitted and actual growth rates is less than 5% over the considered (u, u') domain. The maximum difference is

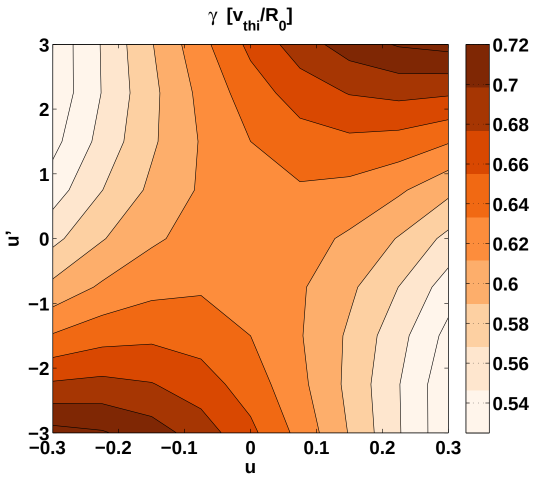

FIG. 1: Linear mode growth rate at $k_\theta \rho_i = 0.4$ as a function of the toroidal rotation u and parallel flow shear u' for the Waltz standard case.

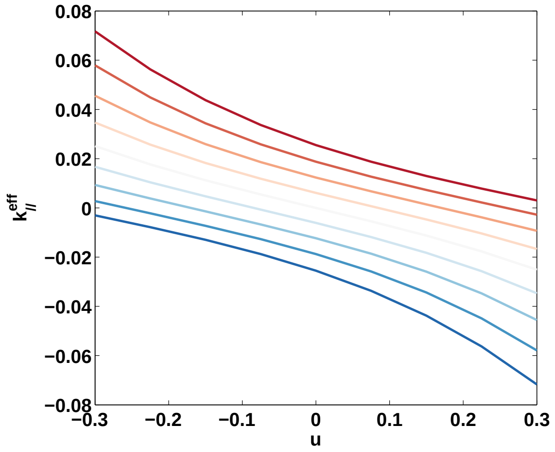

FIG. 2: Effective parallel wave vector at $k_\theta \rho_i = 0.4$ for the Waltz standard case as a function of the toroidal rotation u for increasing parallel flow shear u' (from -3 in blue to +3 in red, with steps of 0.75). Note the change of slope for $uu' < -0.6$.

Cases	1	2	3	4	5
u	0	0.3	0	0.3	-0.3
u'	0	0	3	3	3

TABLE II: Toroidal flow and parallel flow shear values used to compute the coefficients in Eq. (31).

obtained in the top-left and bottom right corners (up to 5% for $uu' < -0.6$) and in the top-right and bottom-left corners (up to 3.5% for $uu' > 0.6$). In the remaining part ($|uu'| < 0.6$) the relative difference is less than 2%. The comparatively worst fit accuracy in the corners of the domain ($|uu'| > 0.6$) is not totally surprising considering that when entering these regions the mode growth rate and frequency deviate increasingly from the value at $u = 0$ and $u' = 0$, therefore breaking one of the assumption of the fluid model. In addition, for $uu' < -0.6$, the variation of the parallel wave vector with u and u' gets stronger, Fig. 2, whereas a constant linear dependence on u and u' over the whole domain was assumed in Eq. (31). In Fig. 2, the effective parallel wavevector is computed as

$$k_\parallel^{\mathrm{eff}} = \frac{\sum k_\parallel |\phi_{k_\parallel}|^2}{\sum |\phi_{k_\parallel}|^2} \tag{32}$$

where the spectral components $\phi_{k_\parallel}$ are obtained from the Fourier transform of the electrostatic potential in the parallel direction. The values shown in the figure are normalised according to the fluid model conventions.

The relative impact of the toroidal rotation and parallel flow shear contributions (b_u and $b_{u'}$, respectively) and of the cross-term ($b_{uu'}$) on the mode growth rate are shown in Fig. 3 as a function of the local inverse aspect ratio ϵ, the safety factor q, the magnetic shear $\hat{s}$, the poloidal wavevector $k_\theta \rho_i$, the electron to ion temperature ratio T_e/T_i and the normalised ion temperature gradient R/L_{T_i}. The values of b_u, $b_{uu'}$ and $b_{u'}$ are computed from the five (u,u') pairs given in Table II and normalised to the growth rate value without flow $\gamma_0 = \gamma_{u=0,u'=0}$. Additional 2D scans were performed to check that the fit accuracy remains acceptable over the range of scanned parameters. The relative difference between the fitted and actual growth rate values is less than 5%, except for $q > 4$ and $k_\theta \rho_i > 0.6$ where it reaches about 10%. As for the reference case, the largest differences are obtained for $uu' < -0.6$ and are correlated to large values of $k_\parallel^{\mathrm{eff}}$. Over the whole parameter range, with the exception of the R/L_{T_i} scan that will be discussed separately, b_u is systematically found to be negative (ITG stabilisation for increasing $|u|$), $b_{u'}$ positive (ITG destabilisation for increasing $|u'|$) and $b_{uu'}$ positive (ITG destabilisation for increasing uu'). The strongest stabilisation by toroidal rotation is obtained at high q, high $k_\theta \rho_i$ and low T_e/T_i. The destabilisation by parallel flow shear is particularly enhanced at high $\hat{s}$ values and to a lesser extent at low ε and q values and at low and high $k_\theta \rho_i$ values. The magnitude of the cross-term mostly depends on ε, q an $k_\theta \rho_i$ and increases with these parameters. The R/L_{T_i} scan has the specific feature that a transition from a Trapped Electron Mode (TEM) to an ITG is obtained when increasing R/L_{T_i}. Interestingly the impact of the flows on the mode stability is reversed at the ITG/TEM transition and the b coefficients all change signs. The magnitude of these coefficients gets particularly large close to the mode transition. Just around the transition, i.e. for $R/L_{T_i} \sim 6 - 7$, changing the flow parameters can even trigger a change of the dominant instability (this is why the calculation of the b coefficients was not possible in this region). Deep in the TEM regime, when R/L_{T_i} approaches zero, the impact of u and u' on the mode

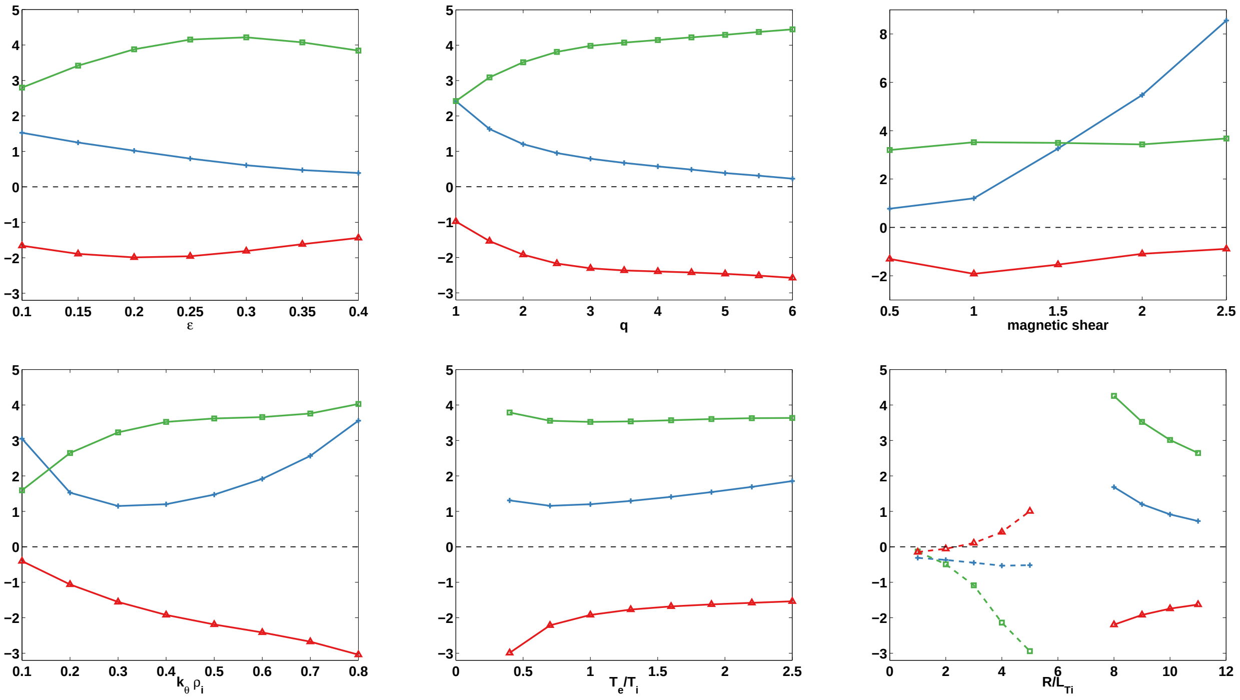

FIG. 3: Normalised coefficients b_u/γ_0 (red), $10b_{uu'}/\gamma_0$ (green) and $100b_{u'}/\gamma_0$ (blue) as a function of the local inverse aspect ratio ϵ, the safety factor q, the magnetic shear $\hat{s}$, the poloidal wavevector $k_\theta\rho_i$, the electron to ion temperature ratio T_e/T_i and the normalised ion temperature gradient R/L_{T_i}. The scans are performed around the reference Waltz standard case. Dashed and full lines indicate that the dominant instability is a TEM or an ITG, respectively.

stability gets vanishingly small.

2. *Shortfall case*

The linear runs for the shortfall cases retain electrostatic and electromagnetic perturbations (ϕ and $A_\parallel$), collisions (pitch-angle scattering only) and flux surface shaping. The Miller parameterisation of the magnetic equilibrium at $r/a = 0.8$ is given in Table III. The most unstable mode is an ITG over the whole spectrum and reaches its maximum growth rate around $k_\theta\rho_i = 0.4$ and $k_r\rho_i = 0$. The impact of the toroidal rotation and parallel flow shear at this wavector is shown in Fig. 4. The first point to note is that even for moderate values of the flow parameters, $-0.3 \le u \le 0.3$ and $-3 \le u' \le 3$, the growth rate variation with respect to the zero flow value can excede ±25%. For small values of $|uu'|$, the flow im-

Miller parameterisation for the DIII-D shortfall case			
s_b	1	s_j	1
κ	1.3621	s_κ	0.2535
δ	0.1917	s_δ	0.3900
ζ	-0.0170	s_ζ	-0.0603
$\partial R_{\rm mil}/\partial r$	-0.1064	$\partial Z_{\rm mil}/\partial r$	0.0708
β'	-0.0277		

TABLE III: Miller parametrisation of the flux surfaces for the DIII-D shortfall case at $r/a = 0.8$. See [14] for the definition of the parameters.

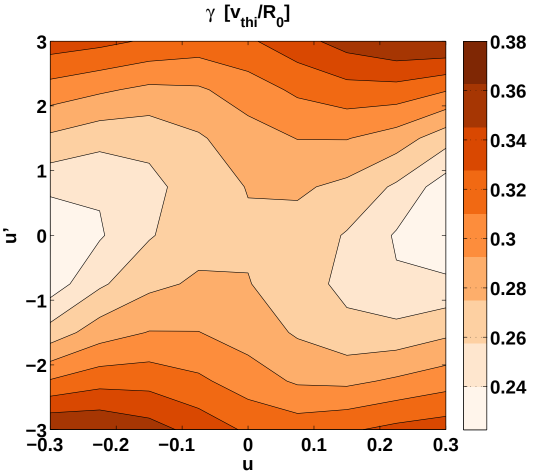

FIG. 4: Linear mode growth rate at $k_\theta\rho_i = 0.4$ as a function of the toroidal rotation u and parallel flow shear u' for the shortfall case.

pact is very similar to what was observed for the Waltz standard case and qualitatively follows the fluid model predictions. However, at larger values of $|uu'|$, the reduction of the mode growth rate at very negative values of uu' is no longer present. This departure from the simple fluid model results is again correlated to large values of $k_{\|}^{\mathrm{eff}}$ and to a change of its dependence on u and u', as shown in Fig. 5. Compared to the Waltz standard case, the $k_{\|}^{\mathrm{eff}}$ values are about 3 times larger, which is mostly due to the higher q and $\hat{s}$ values, and the change of slope of $k_{\|}^{\mathrm{eff}}$ as a function of u and u' occurs earlier when decreasing uu'. The largest $k_{\|}^{\mathrm{eff}}$ values are mirrored by a very strong distortion of the eigenfunctions and a shift of the maximum from the low field side midplane, see Fig. 6 , which makes the failure of a 1-point fluid model in the strong ballooning approximation understandable. As mentioned in the introduction, the importance of the synergy between the plasma flow components for turbulence stabilisation has been realised in the frame of a benchmark exercise based on the DIII-D shortfall case. The focus of the benchmark was on ion-scale turbulence which is why all the non-linear simulations presented in this paper are with $R/L_{T_e} = 0$. Non-linear simulations at finite R/L_{T_e} have not been performed yet, but some insight can be gained by looking at the impact of this parameter on the linear stability results. The variation of the linear growth rate with u and u' has therefore been explored at $R/L_{T_e} = 13.6$ (nominal value) and $R/L_{T_e} = 18$. At $R/L_{T_e} = 13.6$, the most unstable mode is an ITG over most of the domain and the variation of the flow parameters leads to about ±20% changes in the linear growth rate. Qualitatively, the growth rate changes with u and u' are between the results obtained for the Waltz standard case and the shortfall case at $R/L_{T_e} = 0$, i.e. more negative uu' values still tend to be stabilising but not as much as for the Waltz standard case. In the top-left and bottom-right corners, the stabilisation of the ITG leads to a transition to a TEM (TEM dominated points are indicated by black stars on the left plot of Fig. 7). At $R/L_{T_e} = 18$, the most unstable mode is a TEM over the whole domain and the effect of flows gets reversed as in the R/L_{T_i} scan of Fig. 3. The variation of the growth rate with u and u' also gets smaller and is about ±10% with respect to the case without flows. When the linear spectrum is ITG dominated at low $k_\theta \rho_i$ and TEM dominated at high $k_\theta \rho_i$, as for the shortfall case at nominal R/L_{T_e}, a partial compensation of the flow effect could therefore potentially occur in non-linear simulations. This point would deserve further investigation in future studies.

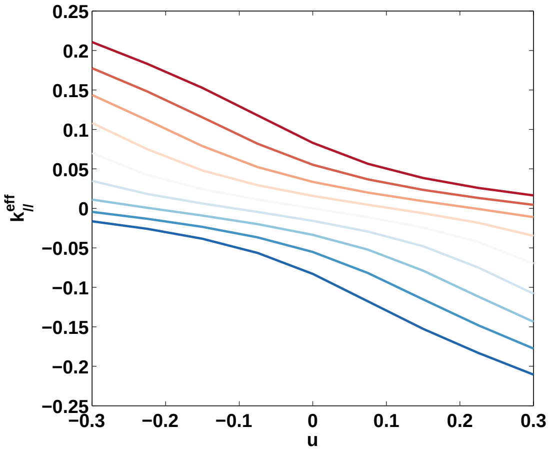

FIG. 5: Effective parallel wave vector at $k_\theta \rho_i = 0.4$ for the shortfall case as a function of the toroidal rotation u for increasing parallel flow shear u' (from -3 in blue to +3 in red, with steps of 0.75).

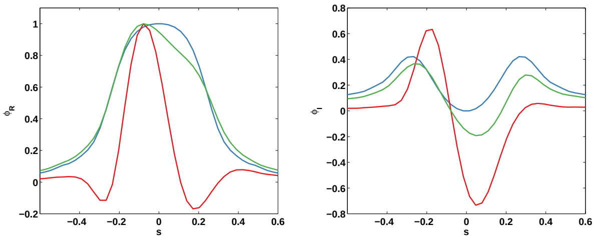

FIG. 6: Parallel structure of the electrostatic potential (real part on the left and imaginary part on the right) for the shortfal case at $k_\theta \rho_i = 0.4$, shown for $u = 0$ and $u' = 0$ (blue curve), $u = 0.3$ and $u' = 3$ (green curve) and $u = -0.3$ and $u' = 3$ (red curve). The parallel coordinate s is zero at the low field side midplane and ±0.5 at the high field side midplane.

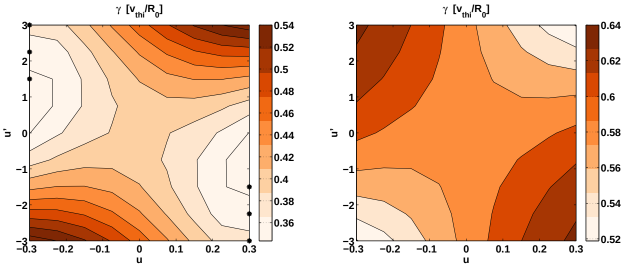

FIG. 7: Linear mode growth rate at $k_\theta \rho_i = 0.4$ as a function of the toroidal rotation u and parallel flow shear u' for the shortfall case at $R/L_{T_e} = 13.6$ (left plot) and $R/L_{T_e} = 18$ (right plot).

Finally, eventhough the toroidal rotation is moderate, centrifugal effects are not totally negligible and, as shown in Fig. 8, tend to increase by some 10% the destabilising effect of parallel flow shear at high $|u|$ values.

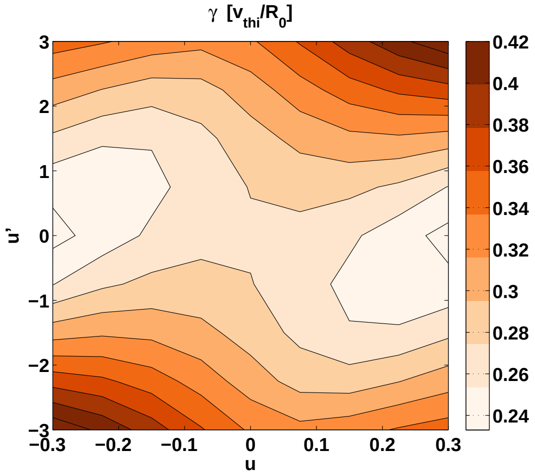

FIG. 8: Linear mode growth rate at $k_\theta \rho_i = 0.4$ as a function of the toroidal rotation u and parallel flow shear u' for the shortfall case with centrifugal effects included.

IV. NON-LINEAR SIMULATIONS

A. Simulations set-up

The non-linear simulations focus on the shorfall case at $R/L_{T_e} = 0$ and investigate the impact of plasma flows by varying u, u' and γ_E around their nominal values. The simulations are performed for kinetic electron and deuterium species with their actual mass ratio $m_e/m_i = 2.72 \times 10^{-4}$. The 5D computational domain is discretised with $N_s = 32$ points in the direction parallel to the magnetic field line (finite differences), $N_{k_\theta} \times N_{k_r} = 21 \times 339$ wavevectors in the perpendicular plane (spectral decomposition) and $N_\mu \times N_{v_\parallel} = 16 \times 64$ points in velocity space. The 21 poloidal wavevectors range from $k_\theta \rho_i = 0$ to 1.3626 (for the reference case, the linear growth rate is zero for $k_\theta \rho_i > 0.8$) and the radial wavevectors extend up to $k_r \rho_i = \pm 24.2457$. For the runs presented in this section, the electrostatic potential perturbation is more than 600 times smaller at the maximum $k_r \rho_i$ than at $k_r \rho_i = 0$, which guarantees that the numerical scheme used to describe $\mathbf{E} \times \mathbf{B}$ shearing (wavevector remapping) is applicable. To minimize the simulation duration, the $\mathbf{E} \times \mathbf{B}$ shearing is only applied after the non-linear overshoot. The simulations are run until a converged time average is obtained, starting after the overshoot or after the $\mathbf{E} \times \mathbf{B}$ shearing is turned on. Depending on the case, the required simulation duration ranges between 400 and $900 R_0/v_{\rm thi}$. A typical case is illustrated in Fig. 9, showing the time evolution of the ion and electron heat fluxes, the convergence of the time averaged fluxes and the time average of $< \sum_{k_r} |\phi(k_r, k_\theta)|^2 >$ as a function of the poloidal wavevector. The electrostatic heat fluxes are defined as:

$$Q_s^r = \left\langle \int \frac{1}{2} m_s v^2 \delta \mathbf{v}_E \cdot \nabla r \, \delta f_s \mathrm{d}\mathbf{v} \right\rangle \tag{33}$$

where $\delta \mathbf{v}_E$ and δf_s are the perturbed $\mathbf{E} \times \mathbf{B}$ velocity and distribution function, respectively, and normalised as:

$$Q_{N,s} = \frac{Q_s^r}{n_s T_s \rho_*^2 v_{\rm thi}} \tag{34}$$

The heat flux due to the magnetic flutter is less than 1% in all the cases considered here and therefore neglected. For comparison with other works based on the shortfall case, e.g. [10, 22, 23], the dimensional fluxes can be calculated from the following normalising factors: 526.43 W.m^{-2} for the ion heat flux and 448.42 W.m^{-2} for the electron heat flux. The radial derivative of the plasma volume, sometimes used to make the fluxes independent of the radial coordinate definition, is $\partial \mathcal{V}/\partial r = 44.615\,\mathrm{m}^2$ at $r/a = 0.8$.

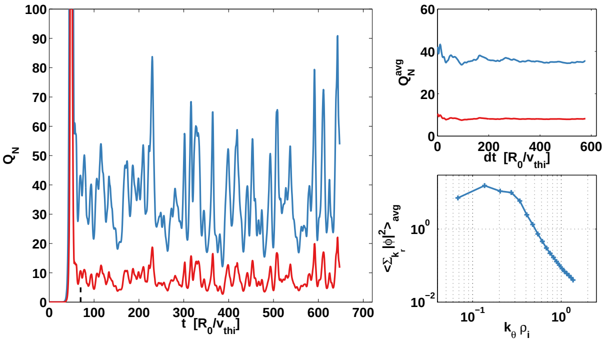

FIG. 9: Shortfall case with $\gamma_E = 0$. Left: time evolution of the ion (blue) and electron (red) normalised heat flux. The vertical black dashed line indicates the starting point for the time averages. Top right: time averaged ion and electron heat fluxes for increasing time average interval. Bottom right: time averaged electrosatic potential spectrum (for the largest time interval).

B. Stabilisation by toroidal rotation

The impact of toroidal rotation is first explored at finite parallel flow shear, $u' = -1.2584$, and zero $\mathbf{E} \times \mathbf{B}$ shear flow. Increasing the toroidal rotation from negative to positive values has first almost no effect and then results into a nearly monotonic decrease of the non-linear ion heat flux, see Fig. 10. The heat flux is about 30% smaller at $u = 0.3$ compared to $u = -0.15$. Qualitatively similar results are obtained at finite $\mathbf{E} \times \mathbf{B}$ shear flow, $\gamma_E = -0.2106$, but with an enhanced effect of toroidal rotation. In the presence of $\mathbf{E} \times \mathbf{B}$ shearing, increasing the toroidal rotation reduces the heat flux by more than a factor of two. The behaviour of the electron heat flux closely follows the one of the ion heat flux (i.e. Q_e/Q_i remains

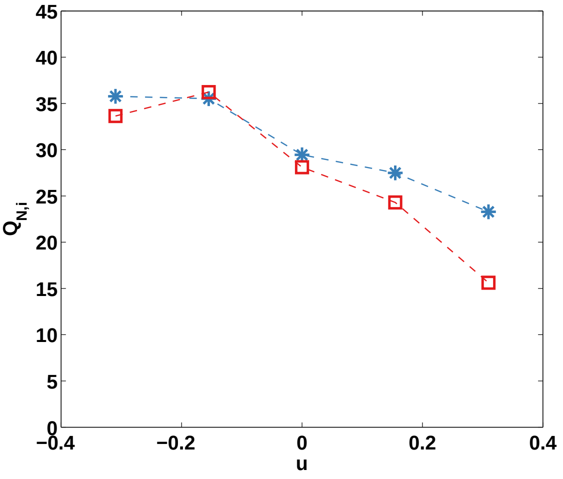

FIG. 10: Time averaged normalised ion heat flux as a function of toroidal rotation for non-linear simulations of the shortfall case with $\gamma_E = 0$ (blue stars) and $\gamma_E = -0.2106$ (red squares). The parallel flow shear is kept at its nominal value $u' = -1.2584$.

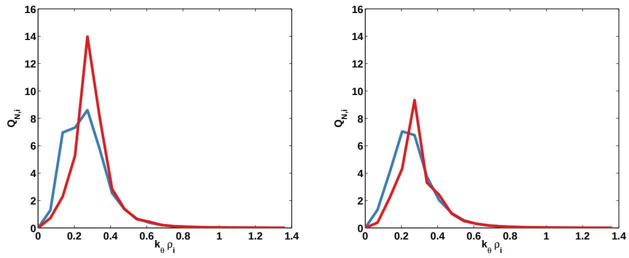

FIG. 11: Time averaged ion heat flux spectra, integrated over the k_r direction, as a function of $k_\theta \rho_i$ for $\gamma_E = 0$ (blue) and $\gamma_E = -0.2106$ (red). Left plot: $u = -0.1549$. Right plot: $u = 0.1549$.

almost constant). Surprisingly, at the nominal toroidal rotation $u = -0.1549$, turning on the $\mathbf{E}\times\mathbf{B}$ shearing has almost no impact on the ion heat flux, whereas a decrease of the transport level is usually expected and in fact observed at the other toroidal rotation values. Looking at the ion heat flux spectrum reveals that $\mathbf{E}\times\mathbf{B}$ shearing has a strong impact, as expected, but that the reduction of the heat flux at $k_\theta \rho_i < 0.25$ is compensated by an increase of the heat flux at $0.25 < k_\theta \rho_i < 0.4$. For $u = -0.1549$, left plot of Fig. 11, this compensation is almost perfect and no effect is seen on the total heat flux. For the other cases, as for instance $u = 0.1549$ in the right plot of Fig. 11, the heat flux reduction at low $k_\theta \rho_i$ is larger than the increase at high $k_\theta \rho_i$ and overall the $\mathbf{E}\times\mathbf{B}$ shearing results in a smaller heat flux. The peak of the time averaged electrostatic potential spectrum, defined as

$$k_\alpha \rho_i^{\mathrm{peak}} = \frac{\sum_{k_r,k_\theta} k_\alpha |\phi(k_r,k_\theta)|^2}{\sum_{k_r,k_\theta} |\phi(k_r,k_\theta)|^2} \tag{35}$$

with k_α standing for k_r or k_θ, does not depend significantly on the toroidal rotation but is shifted towards higher $k_r \rho_i$ and $k_\theta \rho_i$ when $\mathbf{E}\times\mathbf{B}$ shearing is applied, Fig. 12. The linear mode growth rate for the wavevectors around the peak location is shown as a function of the toroidal rotation in Fig. 13. It is interesting to note the similarity between the response of the linear growth rate at the peak of the non-linear spectrum (Fig. 13) and the non-linear fluxes (Fig. 10) to an increase of toroidal rotation. This similarity suggests that the non-linear behaviour finds its root in the linear stability response to toroidal rotation. Quantitatively, the impact on the non-linear fluxes is however much larger than on the linear mode growth rate (more than 5 times). The reason of the stronger impact observed in non-linear simulations is not understood yet.

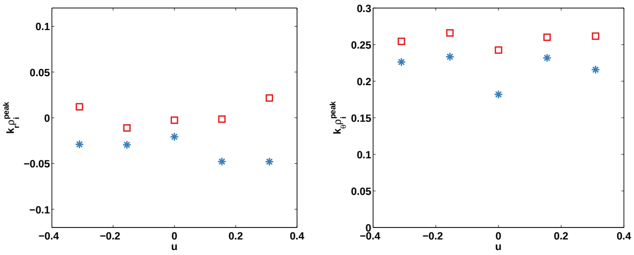

FIG. 12: Position of the peak of the electrostatic potential as a function of toroidal rotation for non-linear simulations of the shortfall case with $\gamma_E = 0$ (blue stars) and $\gamma_E = -0.2106$ (red squares).

C. Impact of the parallel and perpendicular flow shears at finite toroidal rotation

We now turn our attention to the impact of the parallel and perpendicular flow shears in the presence of a finite toroidal rotation. The toroidal rotation is kept fixed at its nominal value and the parallel flow shear is scanned for three values of the $\mathbf{E}\times\mathbf{B}$ shear flow. As shown in Fig. 14, the heat flux response to an increase of u' strongly depends on the value of γ_E. At the nominal value, $\gamma_E = -0.2106$, the heat flux decreases linearly with increasing u'. This reduction is large and the heat flux is almost reduced by a factor of 3 by simply reversing the parallel flow shear. In contrast, at $\gamma_E = 0.2106$, there is almost no dependence of the heat flux on the parallel flow shear. The response at $\gamma_E = 0$ lies between this two extremes and a moderate stabilisation with increasing parallel flow shear is obtained. Focusing on the three cases consistent with the purely toroidal flow assumption (thick symbols in Fig. 14), the heat flux level

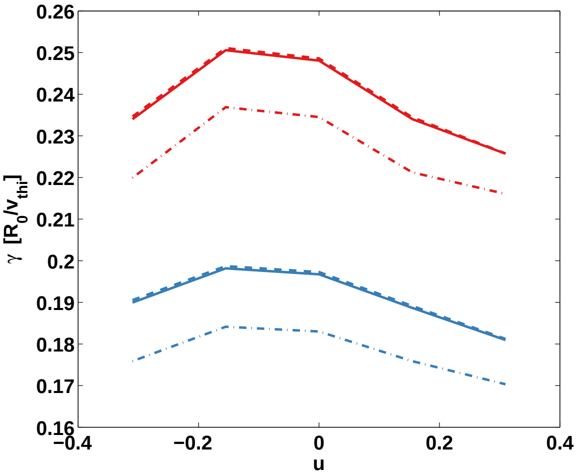

FIG. 13: Linear mode growth rate as a function of toroidal rotation u for the shortfall case at $k_\theta\rho_i = 0.2044$ (blue) and $k_\theta\rho_i = 0.2725$ (red). Dashed lines correspond to $k_r\rho_i = -0.05$, full lines to $k_r\rho_i = 0$ and dashed-dotted lines to $k_r\rho_i = 0.05$.

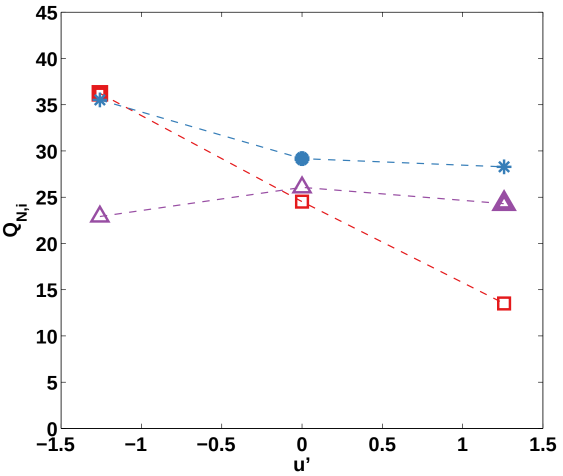

FIG. 14: Time averaged normalised ion heat flux as a function of the parallel flow shear u' in non-linear simulations of the shortfall case with $\gamma_E = -0.2106$ (red squares), $\gamma_E = 0$ (blue stars) and $\gamma_E = 0.2106$ (purple triangles). The toroidal rotation is kept at its nominal value $u = -0.1549$. The thicker symbols indicate the three cases consistent with the assumption of purely toroidal sheared flows.

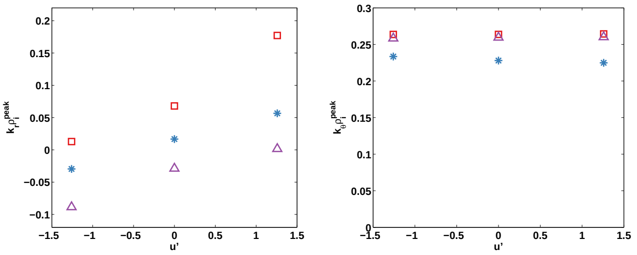

FIG. 15: Position of the peak of the electrostatic potential as a function of the parallel flow shear u' in non-linear simulations of the shortfall case with $\gamma_E = -0.2106$ (red squares), $\gamma_E = 0$ (blue stars) and $\gamma_E = 0.2106$ (purple triangles).

is observed to be asymmetric with respect to a reversal of the parallel and perpendicular flow shears. This asymmetry is due to the finite toroidal rotation and results in a decrease of the ion heat flux by about 35% when the parallel and perpendicular flow shears are reversed. As in the previous section, the peak of the time averaged electrosatic potential is affected by $\mathbf{E}\times\mathbf{B}$ shearing. The peak position moves towards more negative $k_r\rho_i$ values when γ_E increases and to more positive $k_\theta\rho_i$ values at finite $|\gamma_E|$. The parallel flow shear has a an effect on $k_r\rho_i^{\text{peak}}$ comparable in magnitude, but in the opposite direction, whereas it barely affects $k_\theta\rho_i^{\text{peak}}$. These dependencies are summarised in Fig. 15. The non-linear heat flux variations with respect to γ_E and u' again qualitatively follow the linear growth rate variations when computed at the non-linear electrostatic potential peak, see Figs 14 and 16. As for toroidal rotation, the variation of the non-linear heat fluxes is much larger than the one of the linear growth rate. Finally, the ion heat flux is shown in Fig. 17 as a function of the time averaged electrostatic potential perturbation amplitude, $|\phi|_{\text{noZF}}$, for all the non-linear simulations based on the reference shortfall case. The potential amplitude is calculated without the radial

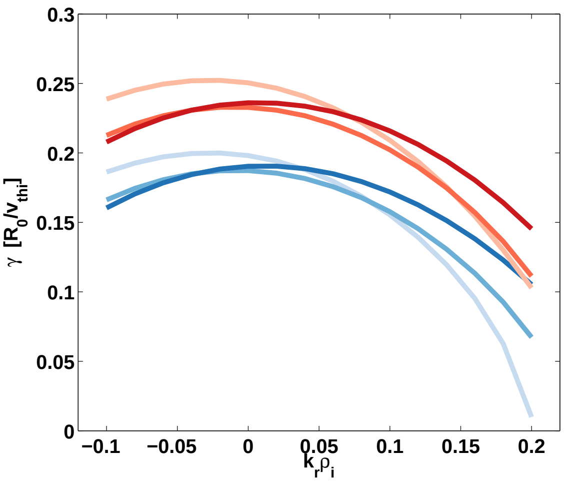

FIG. 16: Linear mode growth rate as a function of the radial wave vector $k_r\rho_i$ for the shortfall case at $k_\theta\rho_i = 0.2044$ (blue) and $k_\theta\rho_i = 0.2725$ (red) for increasing values of the parallel flow shear $u' = -1.2584$ (light), $u' = 0$ (intermediate) and $u' = 1.2584$ (dark).

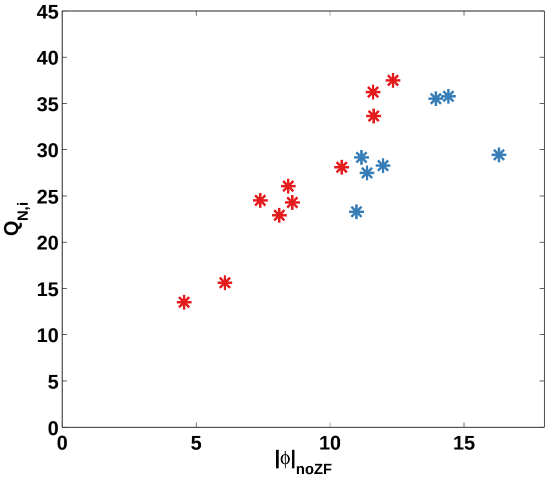

FIG. 17: Time averaged normalised ion heat flux as a function of the total electrostatic potential perturbation amplitude without the contributions of radial modes, for all the non-linear simulations based on the shortfall reference case. Cases with and without $\mathbf{E} \times \mathbf{B}$ shearing are shown in red and blue, respectively.

mode contributions:

$$|\phi|_{\mathrm{noZF}} = \sqrt{\int_{k_\theta \neq 0} |\phi(k_r, k_\theta)|^2 \, dk_r \, dk_\theta} \qquad (36)$$

The linear increase of the ion heat flux with $|\phi|_{\mathrm{noZF}}$ shows that the main impact of flows is not a modification of the cross-phase between temperature and electrostatic potential fluctuations, but rather a change of the non-linear saturation level.

V. CONCLUSIONS

The impact of toroidal rotation u and parallel flow shear u' on the linear stability of the toroidal ITG has been investigated in the frame of a simple fluid model. The key role played by the Coriolis drift and the parallel dynamics in coupling density and parallel velocity perturbations has been highlighted and the linear growth rate shown to have a quadratic dependence on u and u', with a cross-term proportional to uu'. As a consequence, the toroidal rotation and the parallel flow shear can have a stabilising or a destabilising effect, depending on their respective sign and of the magnitude of the cross-term. Guided by the fluid model results, linear gyrokinetic simulations have been performed to determine the scaling of the cross-term with respect to plasma parameters. The strongest growth rate dependence on the cross-term is obtained at high safety factor q, high local inverse aspect ratio ε, high poloidal wavevector $k_\theta \rho_i$ and close to the ITG/TEM transition. Interestingly, the growth rate dependence on u and u' is found to reverse sign at the ITG/TEM transition. The strong interplay between u and u' has been confirmed in non-linear simulations based on the DIII-D shortfall case at $r/a = 0.8$ and with $R/L_{T_e} = 0$. The flow effect on the non-linear fluxes qualitatively follows the linear growth rate variations but with a much stronger amplitude. Adding $\mathbf{E} \times \mathbf{B}$ shearing brings another parallel symmetry breaking term into the game, which can enhance or reduce the turbulence level depending on its sign with respect to u and u'. Qualitatively, the strongest impact is obtained when the different terms conjugate to generate a large parallel symmetry breaking (for instance $u > 0$, $u' < 0$ and $\gamma_E > 0$). The most striking effect observed in the non-linear simulations is the factor of three reduction of the ion heat flux obtained when reversing the parallel flow shear and keeping u and γ_E at their nominal values.
The relevance of this mechanism in the experiments depends on the ability to decouple the flow parameters. In the limit of purely toroidal flows, u' and γ_E are strictly proportional. This proportionality is broken when the poloidal rotation and the pressure gradient make a significant contribution to the radial electric field which is typically the case in transport barriers or close to the plasma edge. Decoupling u from the flow shear is to some extent easier to achieve: increasing the ripple magnitude in the presence of central NBI heating [24] or moving the X-point location from the inboard to outboard side of the vacuum chamber [25] provides an effective way to change the value of the toroidal rotation at relatively constant parallel flow shear by acting on the boundary condition. There are therefore experimental conditions in which the sign dependent interaction of flows in turbulent transport stabilisation evidenced in this theoretical study is expected to be significant. It may in fact be a relevant candidate to interpret the so far unexplained dependence of the ExB quenching strength on toroidal rotation in JET [26] or the dependence of ITBs strength on the direction of toroidal rotation in JT60U [27].

Acknowledgments

The authors would like to thank C. Bourdelle, J. Citrin, G. Dif-Pradalier, D. Escande, N. Dubuit, T. Görler, W. Guttenfelder, C. Holland, M. Honda, E. Narita and G. Staebler for many stimulating discussions from which this work has greatly benefited. The simulations were carried out using HPC resources from GENCI-IDRIS (Grant i2015057398), from the project Equip@Meso (ANR-10-EQPX-29-01) at Aix-Marseille and from the HELIOS supercomputer system at International Fusion Energy Research Centre, Aomori, Japan. This work was partially carried out with funding from the RCUK Energy Programme [grant number EP/I501045].

Appendix A: Inertial effects in GKW

In the rotating frame, the inertial effects appear through the Coriolis and centrifugal drifts:

$$\mathbf{v}_{\text{co}} = \frac{2m_s v_\parallel}{Z_s eB}\mathbf{\Omega}_\perp \tag{A1}$$

and

$$\mathbf{v}_{\text{cf}} = -\frac{m_s\Omega^2 R}{ZeB}\mathbf{b}\times\nabla R \tag{A2}$$

where $v_\parallel$ is the parallel velocity coordinate in the rotating frame and $\mathbf{\Omega}_\perp = \mathbf{\Omega} - (\Omega\cdot\mathbf{b})\mathbf{b}$ with $\mathbf{b}$ the unit vector in the direction of the magnetic field $\mathbf{B}$ and $\mathbf{\Omega} = R\Omega\nabla R\times\nabla\varphi$. There are two important differences between the Coriolis and centrifugal forces. First, the Coriolis force depends on the parallel velocity coordinate $v_\parallel$, whereas the centrifugal force does not. Starting from a density perturbation extended along the magnetic field line and with zero fluid velocity, the Coriolis drift will therefore split the particles according to their parallel velocity and generate parallel fluid velocity perturbations. This is the reason why the Coriolis drift plays a central role in the turbulent transport of parallel momentum [28]. Second, unlike the Coriolis force, the centrifugal force contributes to the parallel acceleration (because it is not perpendicular to the parallel motion). The corresponding modification of the parallel force balance gives rise to poloidal asymmetries in the equilibrium density and electrostatic potential [13]:

$$n_s = n_{R_0,s}\exp\left[-\mathcal{E}_s/T_s\right] \tag{A3}$$

where $n_{R_0,s}$ is the density of species s at the reference major radius R_0 and the energy $\mathcal{E}_s$ is defined as

$$\mathcal{E}_s = Z_s e\Phi^{(1)} - \frac{1}{2}m_s\Omega^2(R^2 - R_0^2) \tag{A4}$$

The poloidally varying electrostatic potential $\Phi^{(1)}$ arises to balance the charge separation caused by the centrifugal force acting on plasma constituents of different mass and is solution of $\Sigma_s Z_s n_s = 0$.

In GKW, the impact of the centrifugal force on the equilibrium is taken into account by specifying the Maxwellian background distribution function as:

$$\begin{aligned} F_{M,s} &= \exp\left[-\frac{Z_s e\Phi^{(1)}}{T_s} - \frac{m_s[\Omega+\omega_s^f]^2}{2T_s}(R^2 - R_0^2)\right] \\ &\times \frac{n_{R_0,s}}{\pi^{3/2}v_{\text{ths}}^3}\exp\left[-\frac{m_s[v_\parallel - (F/B)\omega_s^f]^2}{2T_s} - \frac{\mu_s B}{T_s}\right] \end{aligned} \tag{A5}$$

where $\mu_s = m_s v_\perp^2/B_0$ and $\omega_s^f = \omega_s - \Omega$ is the toroidal angular frequency of species s in the rotating frame. By assumption, $\omega_s^f(r_0) = 0$ for all species and the Maxwellian background is then given by:

$$F_{M,s} = \frac{n_{R_0,s}}{\pi^{3/2}v_{\text{ths}}^3}\exp\left[-\frac{m_s v_\parallel^2}{2T_s} - \frac{\mu_s B}{T_s} - \frac{\mathcal{E}_s}{T_s}\right] \tag{A6}$$

The radial gradient of the Maxwellian enters the gyrokinetic equation, but part of it cancels with other terms. The remaining contribution is noted $\nabla_p F_{M,s}$ in GKW reference papers. Centrifugal effects require the following contribution to be added to $\nabla_p F_{M,s}$:

$$\nabla_p F_{M,s}|_{cf} = \left[\frac{\mathcal{E}_s}{T_s^2}\frac{\partial T_s}{\partial r} + \frac{m_s\Omega}{T_s}(R^2 - R_0^2)\frac{\partial\omega_s^f}{\partial r}\right]F_{M,s} \tag{A7}$$

In addition to the modification of the equilibrium, the effect of the inertial forces on the equations of motion is taken into account by considering the following extra contributions to the gyro-centers velocity and parallel acceleration:

$$\begin{aligned} \left.\frac{d\mathbf{X}}{dt}\right|_{co} &= \mathbf{v}_{\text{co}} & \text{(A8)} \\ \left.\frac{d\mathbf{X}}{dt}\right|_{cf} &= \mathbf{v}_{\text{cf}} + \frac{\mathbf{b}\times\nabla\Phi^{(1)}}{B} & \text{(A9)} \\ m_s v_\parallel\left.\frac{dv_\parallel}{dt}\right|_{cf} &= -\frac{d\mathbf{X}}{dt}\cdot\nabla\mathcal{E}_s & \text{(A10)} \end{aligned}$$

The centrifugal contribution to the parallel acceleration, Eq. (A10), enhances the low field side trapping and is responsible for an enhanced destabilisation of the trapped electron mode at high toroidal rotation [8].

To summarize, GKW takes into account the inertial effects due to the lowest order neoclassical flows, i.e. a purely toroidal rotation of constant angular frequency on a flux surface that is independent of the species. Practically, this is achieved by formulating and solving the equations in the frame rotating at the plasma angular frequency. In this frame, the gyrokinetic equations are modified as follows. The Coriolis force results in the addition of the Coriolis drift to the gyro-center velocity. The centrifugal force results in the modification of the background equilibrium (poloidal asymmetries), in the addition of the centrifugal drift and of the $\mathbf{E}\times\mathbf{B}$ drift due to the first order electrostatic potential to the gyro-center velocity and to the corresponding contribution of these two terms to the parallel acceleration.

Appendix B: Flow shear in GKW

1. Parallel flow shear

The parallel flow shear is implemented as follows in the gradient of the Maxwellian background:

$$\begin{aligned} \nabla_p F_{M,s} &= F_{M,s}\left[\frac{1}{n_{R_0,s}}\frac{\partial n_{R_0,s}}{\partial r}\right. \\ &+ \left(\frac{m_s v_\parallel^2}{2T_s} + \frac{\mu_s B}{T_s} + \frac{\mathcal{E}_s}{T_s} - \frac{3}{2}\right)\frac{1}{T_s}\frac{\partial T_s}{\partial r} \\ &+ \left.\left(\frac{m_s v_\parallel F}{BT_s} + \frac{m_s\Omega}{T_s}[R^2 - R_0^2]\right)\frac{\partial\omega_s^f}{\partial r}\right] \end{aligned} \tag{B1}$$

This implementation assumes that the parallel flow shear is due to the projection of the shear in the toroidal flow and that the species toroidal angular frequency in the rotating frame ω_s^f is constant on a flux surface. The possibility to have a species dependent toroidal angular frequency gradient $\partial\omega_s^f/\partial r$ is retained.

2. E × B flow shear

In the rotating frame, the lowest order $\mathbf{E}\times\mathbf{B}$ flow, $\mathbf{v}_E^f$, is zero at $r=r_0$, by definition of the frame angular frequency. The possibilty to have a finite shear in the $\mathbf{E}\times\mathbf{B}$ velocity is retained and included in the code by expanding $\mathbf{v}_E^f$ around $r=r_0$:

$$\mathbf{v}_E^f(r) = (r-r_0)\frac{\mathbf{b}\times\nabla r}{B}\left.\frac{\partial^2\Phi^f}{\partial r^2}\right|_{r_0} \tag{B2}$$

with Φ^f the lowest order electrostatic potentiel in the rotating frame. The advection of perturbed quantities by the background $\mathbf{E}\times\mathbf{B}$ sheared flow (i.e. terms appearing in the gyrokinetic equation as $\mathbf{v}_E^f\cdot\nabla g$, with g a perturbed quantity) is then treated in Fourier space by a periodic remapping of the radial wavectors [9].

3. Shear flow specification for the modeling of experimental plasmas

Starting from the parallel fluid velocity in the rotating frame:

$$V_{\parallel,s}^f = \hat{u}_{\theta,s}B + \frac{F}{B}\left[s_b\omega_{p,s} + s_b\omega_\Phi - \Omega\right], \tag{B3}$$

the parallel velocity gradient is given by

$$\begin{aligned}\frac{\partial V_{\parallel,s}^f}{\partial r} &= B\frac{\partial\hat{u}_{\theta,s}}{\partial r} + s_b\frac{F}{B}\left[\frac{\partial\omega_{p,s}}{\partial r} + \frac{\partial\omega_\Phi}{\partial r}\right] \\ &+ \hat{u}_{\theta,s}\frac{\partial B}{\partial r} + s_b\omega_{p,s}\frac{\partial F/B}{\partial r}\end{aligned} \tag{B4}$$

By specifying the parallel flow shear of the Maxwellian background in Eq. (B1) with:

$$\begin{aligned}\frac{\partial\omega_s^f}{\partial r} &= \left\langle\frac{B^2}{F}\frac{\partial\hat{u}_{\theta,s}}{\partial r} + s_b\frac{\partial\omega_{p,s}}{\partial r}\right\rangle + s_b\frac{\partial\omega_\Phi}{\partial r} \\ &+ \left\langle\frac{B}{F}\left[\hat{u}_{\theta,s}\frac{\partial B}{\partial r} + s_b\omega_{p,s}\frac{\partial F/B}{\partial r}\right]\right\rangle,\end{aligned} \tag{B5}$$

and by using Eq. (14) to specify γ_E, the departure from a purely toroidal flow is approximately taken into account in the relationship between u_s' and γ_E. What is neglected is the variation of the parallel flow shear on a flux surface due to $\hat{u}_{\theta,s}$ and $\omega_{p,s}$.

---

[1] P.W. Terry, Rev. Mod. Phys. **72**, 109 (2000).
[2] R.E. Waltz, R.L. Dewar and X. Garbet, Phys. Plasmas **5**, 1784 (1998).
[3] N. D'Angelo, Phys. Fluids **8**, 1748 (1965).
[4] P.J. Catto, M.N. Rosenbluth and C.S. Liu, Phys. Fluids **16**, 1719 (1973).
[5] R.E. Waltz, G.D. Kerbel and J. Milovich, Phys. Plasmas **1**, 2229 (1994).
[6] J.E. Kinsey, R.E. Walz and J. Candy, Phys. Plasmas **12**, 062302 (2005).
[7] E.G. Highcock *et al.*, Phys. Rev. Lett. **109**, 265001 (2012).
[8] F.J. Casson *et al.*, Phys. Plasmas **17**, 102305 (2010).
[9] A.G. Peeters *et al.*, Comput. Phys. Commun. **180**, 052301 (2009), URL `https://bitbucket.org/gkw/gkw/overview`.
[10] C. Holland *et al.*, Phys. Plasmas **16**, 052301 (2009), URL `https://fusion.gat.com/theory/Shortfall`.
[11] S.P. Hirshman and D.J. Sigmar, Nucl. Fusion **21**, 1079 (1981).
[12] E.A. Belli and J. Candy, Plasma Phys. Control. Fusion **50**, 095010 (2008).
[13] F.L. Hinton and S.K. Wong, Phys. Fluids **28**, 3082 (1985).
[14] URL `http://www.gkw.org.uk/tikiwiki/Manual`.
[15] A.G. Peeters *et al.*, Phys. Plasmas **16**, 042310 (2009).
[16] A.G. Peeters *et al.*, Phys. Plasmas **19**, 099901 (2012).
[17] A.G. Peeters *et al.*, Phys. Plasmas **16**, 062311 (2009).
[18] J. Weiland *et al.*, Nucl. Fusion **49**, 065033 (2009).
[19] Y. Camenen *et al.*, Phys. Plasmas **16**, 012503 (2009).
[20] J.Q Dong and W. Horton, Phys. Fluids B **5**, 1581 (1993).
[21] X. Garbet *et al.*, Phys. Plasmas **9**, 3893 (2002).
[22] J. Chowdhury *et al.*, Phys. Plasmas **21**, 112503 (2014).
[23] T. Görler *et al.*, Phys. Plasmas **21**, 122307 (2014).
[24] P. de Vries *et al.*, Plasma Phys. Control. Fusion **52**, 065004 (2010).
[25] T. S.-D. *et al.*, Phys. Rev. Lett. **114**, 245001 (2015).
[26] I. V. *et al.*, Nucl. Fusion **54**, 093006 (2014).
[27] E. N. *et al.*, Plasma Fusion Res. **10**, 1403019 (2015).
[28] A.G. Peeters *et al.*, Phys. Rev. Lett. **98**, 265003 (2007).